Constraining Properties of Sedimentary Strata Using Receiver Functions: An Example from the Atlantic Coastal Plain of the Southeastern United States

Erin Cunningham*[1,2] and Vedran Lekic[1]

ABSTRACT

Thickness and seismic velocities of sedimentary sequences strongly affect their response during earthquakes, which can prolong and amplify ground motions. We characterize shallow structure of Atlantic Coastal Plain (ACP) sediments using a passive-seismic approach based on high-frequency *P-to-S* receiver functions. We map the site-specific fundamental frequency for 64 USArray Transportable Array stations and confirm that the method yields results similar to those from traditional spectral ratio techniques, with fundamental frequencies between 0.1 and 1 Hz. In addition, using sediment *S*-wave reverberations and *P-to-S* phase arrival times measured directly from the receiver functions, we invert for average *S*- and *P*-wave velocity profiles of the ACP sedimentary strata. We find that V_S increases with depth following a power-law relationship ($V_S \propto \sqrt{z}$) whereas the increase of V_P with depth is more difficult to constrain using converted wave methods; therefore, we choose to use the Brocher (2005) relationship to obtain V_P through a V_P/V_S relationship. Finally, we use the variation of measured *S*-reverberation amplitudes with depth to validate these velocity profiles. These results have implications for seismic shaking across the ACP, which covers large portions of the eastern United States.

KEY POINTS

- We have developed a method for constraining sediment properties using high-frequency receiver functions.
- We present the fundamental frequency and average *S*-wave velocity profile for the Atlantic Coastal Plain.
- The method has promise for characterizing or removing the effects of areally extensive sedimentary sequences.

Supplemental Material

INTRODUCTION

Although situated on a passive margin with infrequent earthquakes, the eastern coastal regions of the United States have potentially substantial risks during an earthquake like that of the 1886 Charleston, South Carolina, earthquake due to large numbers of unreinforced masonry buildings and aging infrastructure. Many densely populated east coast cities lie on Atlantic Coastal Plain (ACP) sediments, which can amplify ground shaking (Hough, 2012; Pratt *et al.*, 2017; Pratt, 2018) (Fig. 1). The large impedance contrast between ACP sediments and underlying bedrock cause incoming seismic waves to become trapped in the sediments and amplified, leading to damaging ground motion (e.g., Field *et al.*, 1990; Fischer *et al.*, 1995; Baise *et al.*, 2016; Yilar *et al.*, 2017). Unlike sedimentary sequences in confined basins such as the Los Angeles or Seattle basins, the ACP strata are nearly flat, are deposited on an erosional surface with a dip of 2° or less, and extend laterally hundreds of kilometers. Therefore, for site response purposes, the ACP strata can be considered flat strata without well-defined edges that can introduce basin-edge effects. In addition, earthquakes occur beneath ACP sediments, as illustrated by the ongoing seismicity in Charleston, South Carolina, region (Chapman *et al.*, 2016) and recent M_w 4.2 Dover, Delaware, earthquake (Kim *et al.*, 2018). Amplification by sediments and matching fundamental frequencies of sedimentary layers with building resonances is likely responsible for the

1. Department of Geology, University of Maryland, College Park, Maryland, U.S.A.; 2. Now at Center for Earthquake Research and Information at University of Memphis, Memphis, Tennessee, U.S.A.

*Corresponding author: E.Cunningham@memphis.edu

Cite this article as Cunningham, E., and V. Lekic (2020). Constraining Properties of Sedimentary Strata Using Receiver Functions: An Example from the Atlantic Coastal Plain of the Southeastern United States, *Bull. Seismol. Soc. Am.* **XX**, 1–15, doi: 10.1785/0120190191

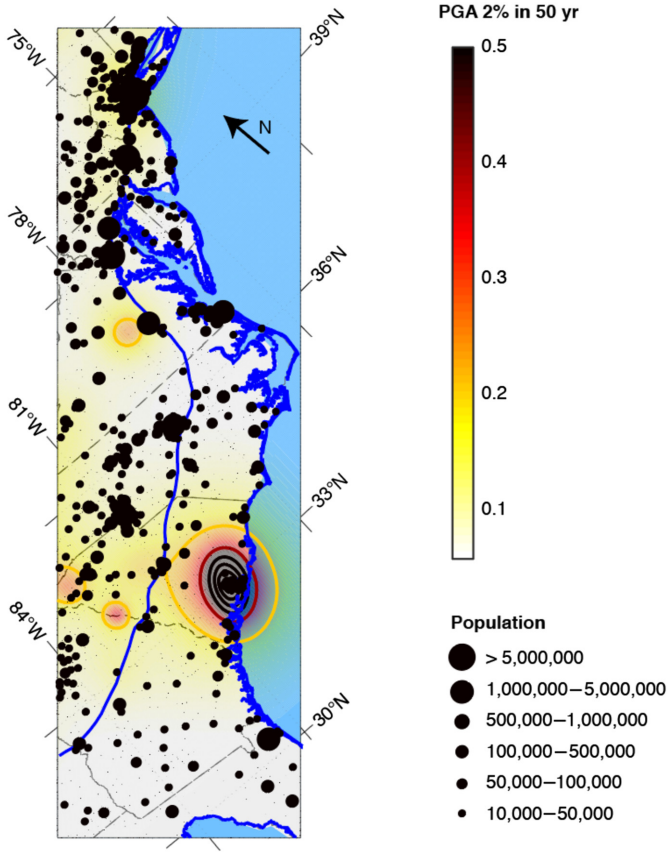

Figure 1. Hazard map of the Atlantic Coastal Plain (ACP) showing locations and populations of cities and towns on top of potential ground shaking. The boundary of the ACP is shown as a thick (blue) line (Fenneman and Johnson, 1946), with population size shown as black circles (Center for International Earth Science Information Network [CIESIN], 2018), and peak ground acceleration (PGA) that has a 2% chance of being exceeded in 50 yr (from USGS 2014 hazard maps, Petersen *et al.*, 2014). The color version of this figure is available only in the electronic edition.

substantial damage resulting from even moderate-size earthquakes on the east coast such as the 2011 M_w 5.8 Mineral, Virginia, earthquake (Hough, 2012; Pratt *et al.*, 2017).

Mapping the fundamental frequency and amplification of thick sedimentary sequences is useful for geoengineering and hazard analyses, as overlap between the fundamental resonant frequencies of sedimentary layers and buildings can be particularly damaging (e.g., Flores *et al.*, 1987). Typically, the average velocity to 30 m depth (V_{S30}) is used as a proxy for site amplification in hazard analyses and ground-motion prediction equations (e.g., Abrahamson and Silva, 2008). These site characterizations by V_{S30} are typically used to inform seismic building codes (e.g., National Earthquake Hazards Reduction Program provisions). However, characterizing only the uppermost 30 m of soil and sediment may not be sufficient to describe damaging site effects, particularly for larger buildings and infrastructure. More recent studies argue that fundamental period, sometimes in combination with a velocity term (e.g., V_{S30}, $Z_{1.0}$ [depth to $V_S = 1$ km/s], or $Z_{2.5}$ [depth to $V_S = 2.5$ km/s]) is a better proxy for site amplification and response and reduces uncertainty in ground-motion prediction equations (Luzi *et al.*, 2011; Pitilakis *et al.*, 2013; Zhao and Xu, 2013).

The large impedance contrast between the bedrock and overlying ACP strata means that the peak amplification should occur at the fundamental frequency of the sedimentary strata (Pratt *et al.*, 2003; Narayan, 2010). Because the ACP strata are relatively thick and flat when compared to those on the west coast (American Association of Petroleum Geologists [AAPG]. Basement RockProject Committee and U.S. Geological Survey, 1967), the fundamental frequency in regions with thicker sediments within the ACP will be low and will influence shaking over large areas. The low-fundamental frequencies of the ACP strata predominantly affect larger structures with matching resonant frequencies (e.g., bridges, tall buildings, and industrial facilities), which is of particular concern for cities situated on the east coast where large buildings and infrastructure were constructed before current seismic building codes were in effect. Thus, it is crucial for hazard analysis to constrain the amplification and fundamental frequencies across the ACP.

Common methods employed to estimate fundamental frequency are the standard spectral ratio (SSR) and the ambient noise or earthquake horizontal-to-vertical spectral ratio (HVSR or E-HVSR, respectively). The SSR technique requires comparing ground motions from earthquakes at a target site located on sediment to a reference on bedrock (e.g., Borcherdt, 1970; Frankel *et al.*, 2002; Pratt *et al.*, 2017; Perron *et al.*, 2018). However, good reference sites with matching underlying bedrock material may not be available for all stations on the ACP, given its large geographic extent and heterogeneous bedrock. Mismatch in the bedrock material between the target and reference sites will degrade the accuracy of the seismic hazard interpretation (Steidl *et al.*, 1996). In contrast, the HVSR techniques do not require a reference station. Instead, HVSR isolates the horizontal response from the vertical at a specific station through spectral division, as horizontally polarized *S* waves will cause the significant most ground shaking during an earthquake (e.g., Nakamura, 1989; Lermo and Chávez-García, 1993; Kawase *et al.*, 2018). In some cases in which available data are sparse and sedimentary strata are thick and the impedance contrast is not particularly high, such as in much of the central and eastern United States, the resonance peak that is used to infer fundamental frequency may not be clear and may prove difficult to interpret (Pratt *et al.*, 2017; Yilar *et al.*, 2017; Yassminh *et al.*, 2019). In the central and eastern United States, dense high-frequency seismic surveys are rare, and so broadband seismic stations may be useful for constraining the fundamental frequency over large regions. However, traditional HVSR techniques for constraining the fundamental frequency of the ACP sedimentary strata may still prove difficult (Yassminh *et al.*, 2019).

Here we propose, validate, and apply a new approach to constrain key sediment properties using high-frequency

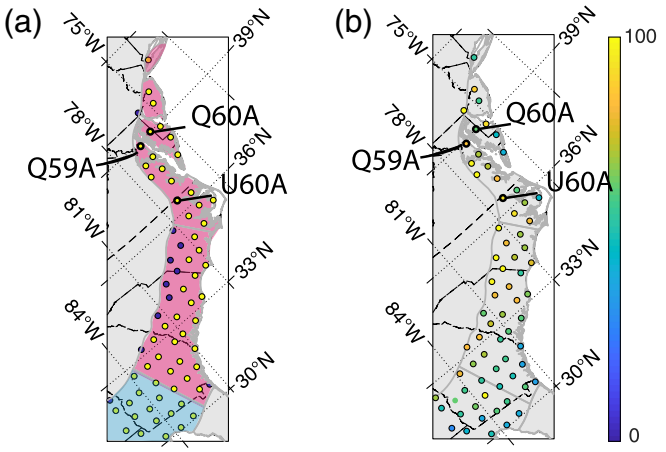

Figure 2. Map of station locations in the ACP used in this study with stations names Q60A, Q59A, and U60A noted as they are example stations used later in this study. (a) Sediment reverberation identification. Circles represent station locations used in this study. Dark (blue) circles indicate stations which no clear sediment reverberations found in the receiver function, whereas lighter (yellow) circles indicate stations where clear sediment reverberations were identified in the receiver function. Based on Fenneman Physiographic Provinces, stations in the southern (cyan) region are grouped in to the eastern gulf (EG) coastal plain (CP) sediments and stations in the northern (pink) region are grouped into CP sediments. (b) Number of receiver function (RF) events used at each station. The color version of this figure is available only in the electronic edition.

P-to-S receiver function (PRF) analyses. PRFs isolate the *S*-wave conversions across a large impedance contrast (product of velocity and density) through deconvolution, similar to H/V (the ratio) techniques. However, PRFs can be analyzed in the time domain in which individual arrivals are readily identified and associated with *S*- or *P*-wave reverberations. Although PRFs are traditionally used to constrain crustal and lithospheric structure, high-frequency PRFs are strongly sensitive to shallow impedance contrasts such as that between thick ACP sediments and bedrock (Zelt and Ellis, 1999; Leahy *et al.*, 2012; Yeck *et al.*, 2013). Therefore, we propose to use measurements of converted *S* waves and reverberations from the high-frequency PRFs calculated for EarthScope USArray Transportable Array (TA) broadband seismic stations to characterize the thicknesses and seismic velocities of ACP strata. We also compare a northern coastal plain (CP) section to one including an eastern gulf (EG) CP section to examine the similarity of the entire ACP (Fig. 2).

Because of the large impedance contrast between ACP sediments and underlying bedrock, strong *S*-wave reverberations are present in the *P*-wave coda. Computing the autocorrelation of the PRFs allows us to easily measure the two-way *S*-wave reverberation time (T_{Ss}) in the thick sediments (Yu *et al.*, 2015; Cunningham and Lekic, 2019), which is directly related to the fundamental frequency of the sediment strata. The fundamental frequency of sediment reverberations is calculated from measurements of T_{Ss} at each broadband seismic station, allowing for a map of sediment fundamental frequency across the ACP to be created.

We find that PRFs can be useful in constraining other sediment properties, including the *S*-wave velocity profile. Assuming T_{Ss} corresponds to the *S*-wave travel time to the base of the sediments along with interpolated sediment thickness at each station (Fig. S1), an average *S*-wave velocity profile of the ACP strata can be inferred. By incorporating the arrival time of one additional phase T_{PPbs}, an average *P*-wave velocity profile should be able to be obtained (Fig. 3). However, we find that measuring T_{PPbs} is challenging at stations with sedimentary thicknesses greater than 1 km. We validate the average *S*-wave velocity profile by comparing predicted reflection coefficients against amplitudes of the measured phase arrivals, because these amplitudes are directly related to the impedance contrast between ACP sediments and the underlying bedrock.

RECEIVER FUNCTION CALCULATIONS

High-frequency PRFs are calculated for 75 broadband seismometers from the EarthScope TA stations located on the ACP of the United States (Fenneman and Johnson, 1946). To calculate PRFs, we use 300 s long windows of three-component waveform data from teleseismic events with $M_w > 5.6$ and epicentral distance between 30° and 90° from each station. The events are quality controlled, extracting those with a minimum Z-to-R cross correlation of 0.3 and a maximum difference of 5 s between the automatically determined *P*-arrival time and prediction for the 1D velocity model ak135 (Kennett *et al.*, 1995), with no requirement on minimum signal-to-noise threshold. (see Data and Resources, Abt *et al.*, 2010). We use a free-surface transform matrix (Kennett, 1991) and find the surface velocity that minimizes the parent amplitude (*P* for PRFs) on the daughter component (*S* for PRFs) to project the waveforms onto the *P–SV–SH* system. We pick the arrival times and apply a fourth-order Butterworth band-pass filter to waveforms of 0.03–4 Hz. We then use the iterative time-domain deconvolution with Gaussian half-amplitude half-width of ~0.12 s to calculate the PFs, which we call 4 Hz PRFs to distinguish them from the more typical, lower frequency 0.03–1 Hz band-pass filtered PRFs (Ligorria and Ammon, 1999). The PRF calculations are preformed using the automated procedure detailed in Abt *et al.* (2010).

The 75 seismic stations within the ACP are further culled to only those that show clear phase arrivals from sediment reverberations in the receiver functions. Following the procedure laid out in Cunningham and Lekic (2019), which determines whether a significant sediment reverberation exists in the PRF. We require that the autocorrelation of the PRF can be sufficiently well fit by a decaying sinusoid—meaning that the PRF displays the oscillatory pattern of sediment reverberations—and that the amplitude of the sediment phase PP_bs is at least

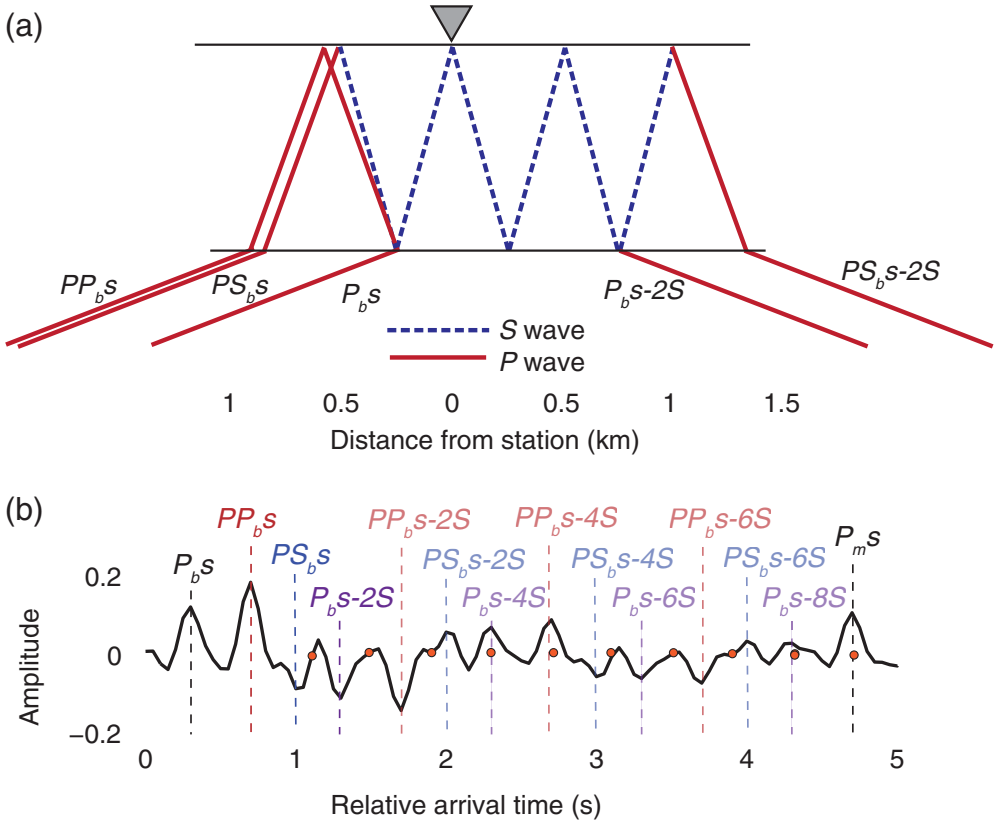

Figure 3. (a) Ray-path geometry of *P-to-S* phases converted across the base of a 0.5 km thick sediment layer, along with the largest amplitude first- and second-order multiples for an incident plane wave of horizontal slowness 0.0789 s/km. (b) Synthetic receiver functions computed for a model with a 0.5 km thick sediment layer and horizontal slowness 0.06 s/km (V_P = 2.5 km/s, V_S = 1 km/s), crustal V_P = 6.2 km/s, V_S = 3.5 km/s, a Moho at 35 km depth, and mantle V_P = 8 km/s, V_S = 4.6 km/s. Direct conversions are in black, whereas the oscillatory pattern is attributed to sediment multiples, labeled in red, blue, and purple. Circles (orange) on the receiver function indicate the expected arrival time of phases with more than 2 P-wave legs would arrive. The color version of this figure is available only in the electronic edition.

30% of the maximum amplitude in the signal. We find that 11 of the stations originally assigned to be in the ACP do not meet this criterion. Stations that are within the ACP but do not have large sediment reverberations at the frequencies analyzed in this study mainly lie on the edge of the ACP, as defined by Fenneman's physiographic provinces, (Fig. 2a) and therefore might be installed in areas with little or no sediment. Alternatively, substantial noise levels can also degrade the signal of sedimentary reverberations on the PRFs. In the end, we obtain a dataset of 64 stations that meet these criteria, containing between 31 and 304 individual PRFs per station (Fig. 2b).

SEDIMENT FUNDAMENTAL FREQUENCY

To map the fundamental frequency of reverberations across the ACP, we measure the two-way *S*-wave travel time in sediment from PRFs at each station. The large impedance contrast between the sediments and basement rocks means that PRFs are particularly sensitive to *S*-wave reverberations. The conversions and reverberations produced from this impedance contrast appear as peaks on the receiver function corresponding to ray paths shown in Figure 3a and relative phase arrival times shown in Figure 3b. In PRFs, the largest amplitude, longest duration oscillatory phases are those that contain two-way *S*-wave reverberations within the sediment (e.g., PS_bs, P_bs-2*S*, PP_bs-2*S*, PS_bs-2*S*, P_bS-4*S*, PP_bs-4*S*, etc.), which dominate the PRF signal. Reverberations arriving at later times in the PRF are dominated by primarily *S*-wave energy because PRFs are computed from upgoing *P* and *S* waveforms estimated using the free-surface transform (Kennett, 1991), which effectively separates *P*- and *S*-wave arrival. Because the *SS* reflection coefficient at the base of the sedimentary strata is large, the *S*-wave reverberations dominate the PRF. Although the *S*-wave reverberation time (T_{Ss}) and amplitude (r_0) can be inferred directly from the PRFs, a more reliable method is to make this measurement on the autocorrelation of the receiver function (Fig. 4; Yu *et al.*, 2015; Cunningham and Lekic, 2019). When a low-velocity layer is present, the autocorrelation of the receiver function will have a large negative peak at reverberation time T_{Ss} and amplitude $-r_0$. Because the *S*-wave reverberations are nearly vertical, the mean PRF at each station can be used to calculate the autocorrelation. We validate this with a synthetic receiver function (Fig. 4a), demonstrating that picking T_{Ss} from the mean PRF agrees with individual *Ps* receiver function (RF) autocorrelations. The measurements of T_{Ss} and $-r_0$ made from the mean PRF are equal to the expected values given the input model. For example stations U60A and Q60A, which lie on regions with different sediment thicknesses, measurements of T_{Ss} and $-r_0$ from the mean PRF are clear, consistent with individual autocorrelations, and have a larger value for T_{Ss} and smaller r_0 with increasing sediment thickness. (Fig. 4b,c).

Measurements of T_{Ss} and r_0 are made for all 64 stations across the ACP. As expected, with increasing sediment thickness toward the coast, T_{Ss} increases (Fig. 5a, Fig. S2a). Thicker sediments will have faster velocities at depth due to

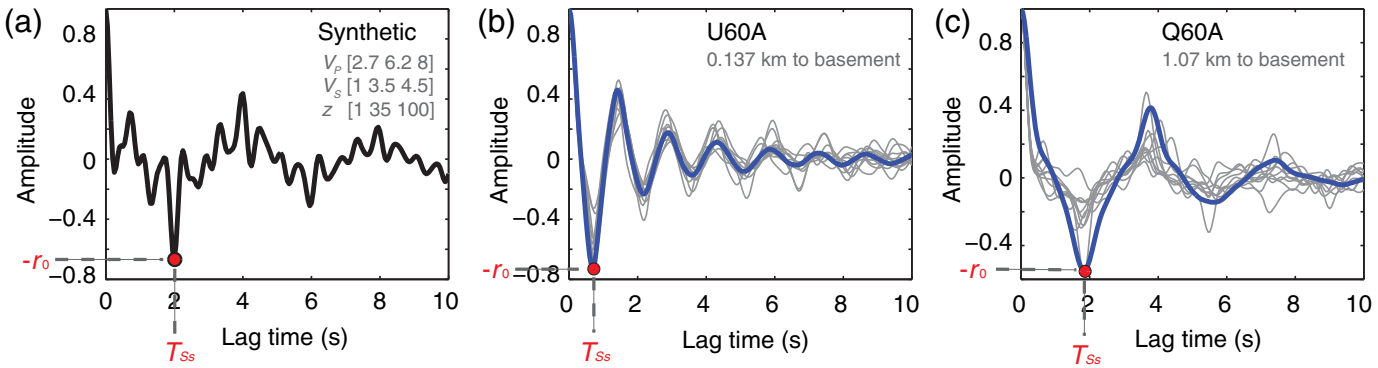

Figure 4. T_{Ss} and r_0 measurements from 4 Hz *Ps* receiver function autocorrelations. With increasing sediment thickness, T_{Ss} increases. (a) Autocorrelation of synthetic RF calculated using spectral division for velocity model described in top right corner. T_{Ss} and r_0 are picked as the first negative large amplitude shown by the dot. (b) Autocorrelation of 4 Hz *Ps* RFs for station U60A located on 0.137 km of sedimentary material. Mean autocorrelation shown as thick (blue) line and a randomly selected subset of the 93 *Ps* RF autocorrelation events shown in gray to demonstrate the variation at each station. T_{Ss} and r_0 pick shown as dot. (c) Autocorrelation of 4 Hz *Ps* RFs for station Q60A located on 1.07 km of sedimentary material. Mean autocorrelation shown as thick (blue) line and a randomly selected subset of the 63 *Ps* RF autocorrelation events shown in gray. T_{Ss} and r_0 pick shown as dot. The color version of this figure is available only in the electronic edition.

compaction, reducing the impedance contrast between sediments and basement rock. Therefore, as sediment thickness increases, r_0 is expected to decrease, consistent with our observations shown in Figure 5b (Fig. S2b).

Assuming that the *S*-wave reverberations are nearly vertical in the slow sedimentary strata, and that the largest impedance contrast corresponds to that between the sediments and bedrock, the relationship between T_{Ss} and fundamental frequency becomes quite simple. The fundamental frequency (F_0) depends on the average *S*-wave velocity (V_S) of the sediment layer and sediment thickness (H_b) in the quarter wavelength approximation (Joyner *et al.*, 1981; Shearer and Orcutt, 1987; van der Baan 2009) as

$$F_0 = \frac{V_S}{4H}. \quad (1)$$

Assuming near-vertical incidence in the low-velocity sediment layer, two-way *S*-wave travel time in sediment (T_{Ss}) is

$$T_{Ss} = 2H_b/V_S, \quad (2)$$

so that fundamental frequency is related to T_{Ss} by:

$$F_0 = \frac{1}{2T_{Ss}}. \quad (3)$$

Assuming vertical incidence introduces errors that are negligible compared to observational uncertainty; for example, the approximation introduces an error of <0.2% (3 ms for a 2 s travel time) in T_{Ss} for the example of a typical incoming *P*-wave ray parameter of 0.05 s/km and a 1 km thick sediment with $V_S = 1$ km/s. Transforming the station measurements of T_{Ss} to F_0 accordingly, we produce a map of site-specific fundamental frequency across the ACP (Fig. 4c) obtaining fundamental frequencies ranging from 1.1 Hz in thin sediments to 0.16 Hz thicker sediments (Fig. S2c).

SEDIMENT VELOCITY PROFILES

Average ACP V_S profile

When the basement depth and fundamental frequency are known, the *S*-wave velocity of the sediment can be found (e.g., Bodin *et al.*, 2001; Parolai *et al.*, 2002; Stephenson *et al.*, 2019). Because of trade-offs between sediment thickness and velocity, inferring the average *S*-wave velocity structure of the ACP using measurements of T_{Ss} requires additional information and assumptions. The most crucial information needed is the sediment thickness at each seismic station estimated from existing studies. Borehole data with estimates of depth to basement along the ACP are available from AAPG (AAPG Basement Map of North America, 1967), aggregates published contour maps of wells penetrating basement rocks to obtain an approximate sediment thickness (Fig. S1). As the ACP strata consist of widespread, nearly horizontal sedimentary strata, we make the assumption that seismic velocities at a given depth will be similar throughout the ACP strata. Pratt (2018) found the ACP velocities at widely spaced seismic arrays were within about 10% of each other despite locations hundreds of kilometers apart, further validating this assumption. This allows for inversion of an average ACP velocity profile rather than requiring that we invert for separate velocity profiles beneath each station. Finally, when constructing velocity profiles parameterized using a power-law relationship, we assume that the seismic velocity in the sediments does not have large increases due to internal layering, that is, we assume V_S increases gradually with depth. These assumptions, along with measurements of T_{Ss} from receiver functions, will allow for an estimation of an average 1D velocity profile for the ACP sedimentary strata.

To invert for the *S*-wave velocity of the ACP, we seek a single velocity profile that minimizes the misfit between predicted and observed T_{Ss} at all stations. We parameterize the velocity

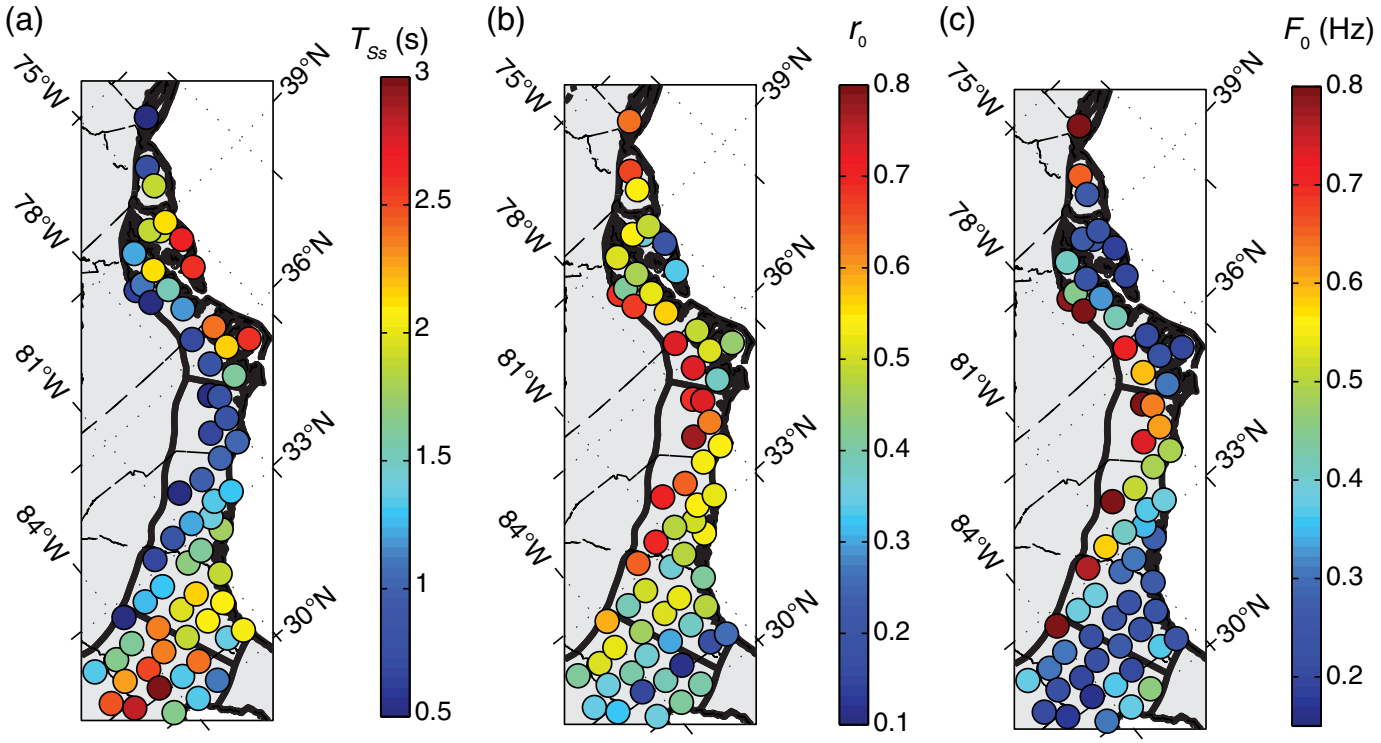

Figure 5. Measurements from the 4 Hz autocorrelated RFs across the ACP. (a) Measurements of T_{Ss} at each station across the ACP. As sediment thickness increases T_{Ss} increases. (b) Measurements of r_0 across the ACP. As sediment thickness increases, the r_0 (related to the impedance contrast) decreases. (c) Fundamental frequency which is related to T_{Ss} as $F_0 = \frac{1}{2T_{Ss}}$ across the ACP. The fundamental frequencies are clipped at 0.8 Hz to highlight the lower frequency variation across the ACP. The color version of this figure is available only in the electronic edition.

profile in two ways: a power-law dependence of V_S with depth and in terms of constant velocity layers. Although velocity profiles parameterized with constant velocity layers are commonplace in seismology, the power-law dependence of V_S with depth parameterization has been found suggested to be a good description in the shallow subsurface (Delgado *et al.*, 2000). An additional advantage of this parameterization is that multiple studies have computed generic surface-wave dispersion and eigenfunction expressions for such velocity profiles (Godin and Chapman, 2001; Tsai and Atiganyanum, 2014). To explicitly account for uncertainty in our measurements, we use a Bayesian inversion framework. To minimize the influence of outliers on the inferred V_S profiles, we define an L1-norm misfit function $\phi_d(m)$for N stations:

$$\phi_d(m) = \sum_{i=1}^{N} \frac{|T_{Ss\,i}^{\mathrm{obs}} - T_{Ss\,i}^{\mathrm{pred}}|}{\varepsilon}, \tag{4}$$

in which $T_{Ss\,i}^{\mathrm{obs}}$ is the observed and $T_{Ss\,i}^{\mathrm{pred}}$ is the model-predicted T_{Ss} at each station i, and ε is the standard deviation of the measurement uncertainty. Based on variations of T_{Ss} observed using different subsets of data, we fix ε to be 0.1 s.

For the power-law parameterization, the predicted T_{Ss} is calculated from equation (2) using the *S*-wave velocity at each depth calculated as

$$V_S(z) = V_0 + a_1(z)^p, \tag{5}$$

in which V_0 is the starting *S*-wave velocity at the surface in meters per second, z is the depth in meters, and a_1 and p are parameters that describe the shape of the power-law dependence of velocity with depth, and $0 < a_1 < 100$ and we fix p to be 0.5, implying a linear increase of shear rigidity with depth (Chapman and Godin, 2001).

For the layered parameterization, the predicted T_{Ss} is calculated from equation (2) using the *S*-wave velocity at each depth calculated as

$$V_S = \begin{cases} V_U, & z < h \\ V_L, & z \geq h \end{cases}, \tag{6}$$

in which V_U and V_L are *S*-wave velocities in the upper and lower layer, respectively, and h is the depth of the interface between them. When inferring h, V_U, and V_L, we assume that $0 < V_U < 2000$ and $0 < V_L < 4000$ m/s. The only assumption on h is that its depth is shallower than the base of the sedimentary strata.

We use a Markov chain Monte Carlo approach computing the log likelihood:

$$L = -N\log(2\varepsilon) - \phi_d, \tag{7}$$

to obtain the best-fit parameter values and map out uncertainties and trade-offs among them.

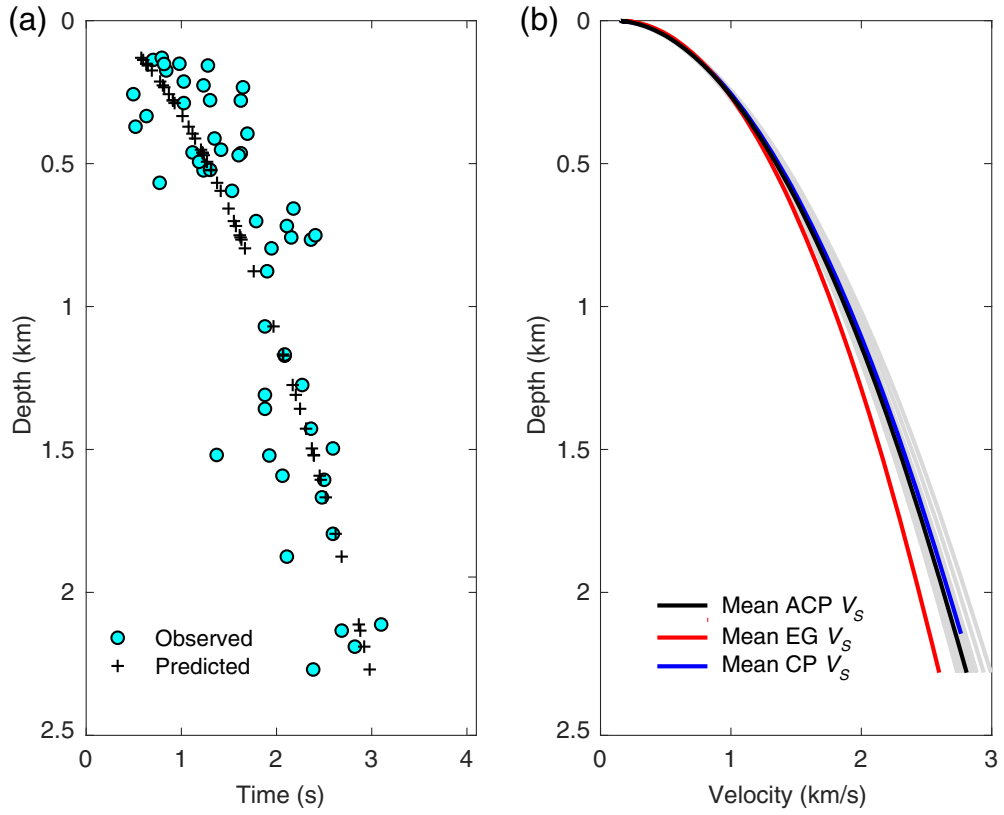

Figure 6. V_S velocity profile from inversion. (a) T_{Ss} measurements from and 4 Hz *Ps* RF (cyan) circles compared to T_{Ss} predicted from the mean V_S profile from our best-fit inversion (black crosses). (b) V_S velocity inversions using T_{Ss} measurements and assuming V_S increases in a power-law fashion with depth. A range of velocity inversions using stations with sediment thickness less than 2.5 km is plotted in gray, and the average of the ensemble of models is plotted in black. The average of the ensemble of profiles obtained by inversion for the stations in the EG CP sediments is plotted lighter red, and for the stations in the CP is plotted in blue. The color version of this figure is available only in the electronic edition.

We find that the average ensemble V_S profile does not adequately predict the measurements of T_{Ss} for sedimentary sequences thicker than about 2.5 km (Fig. S3). The four stations that lie on top of very thick sedimentary sequences (454A, 553A, 554A, and 555A) lie on top of the South Georgia Rift basin, a distinct Mesozoic basin hidden beneath CP sediments (Chowns and Williams, 1983; Daniels *et al.*, 1983; Sartain and See, 1997). We interpret the T_{Ss} picks at these stations to likely be coming from an interface with large impedance contrasts within the CP sediment section (such as between unconsolidated and consolidated sediment) and not from the sediment-basement impedance contrast (or postrift unconformity). Therefore, these points are excluded, and the inversion is performed for stations with a basement depth of less than 2.5 km thick. We choose to perform the inversion using stations that cover the entire ACP, as well as for stations in the EG CP sediments and CP profiles, separately (Fig. 2a). The three resulting V_S profiles match closely (Fig. 6), with the parameters of the inversion remaining similar (Fig. S4). This justifies our assumption of geographic uniformity of velocity at a particular depth within the ACP. Using the values of V_0 and a_1 from the minimum misfit solution yields an equation for V_S velocity (in meters per second) of the ACP sediments as

$$V_S(z) = 100 + 55(z)^{0.5}. \quad (8)$$

The misfit reduction for the V_S power-law inversion for all of the stations above 2.5 km thickness is 8% compared to the stating model in which $a_1 = 50$ and $V_0 = 200$. We also choose to perform V_S velocity inversions for the entire ACP, EG, and CP, assuming two distinct *S*-wave velocity layers (Fig. 7). We find that the velocities obtained in the two-layer model are similar having the same starting and ending velocities with the exception of EG (which has very few stations lie above shallow sedimentary layers).

Average ACP V_P profile

Because the *P* reverberations within the sedimentary column are less prominent than *S* reverberations, constraining the average ACP V_P profile from receiver function data is more difficult. Indeed, because PRFs isolate the *S*-wave conversions from subsurface interfaces, prominent phases always include at least one *S*-wave leg; therefore, the timing of any phase arrival will also depend on the *S*-wave travel time through the sediments. Consequently, inverting for the V_P profile requires not only making an arrival-time measurement on a phase sensitive to the V_P in the sediments, but also involves the same data—measurements of T_{Ss}—and assumptions used for obtaining a V_S profile. Here, we utilize PP_bs, which is generally the largest amplitude phase arrival on the RF that contains a *P*-wave traveling in the sediment (Fig. 8). Assuming near-vertical incidence, the travel time of PP_bs (T_{PPbs}) depends on the sediment thickness (H_b), *P*-wave velocity (V_P), and sediment *S*-wave travel time as

$$T_{PPbs} = \frac{H_b}{V_P} + \frac{1}{2}T_{Ss}. \quad (9)$$

The measurement of T_{PPbs} and the PP_bs phase amplitude is shown for a synthetic receiver function (Fig. 8a) and for two

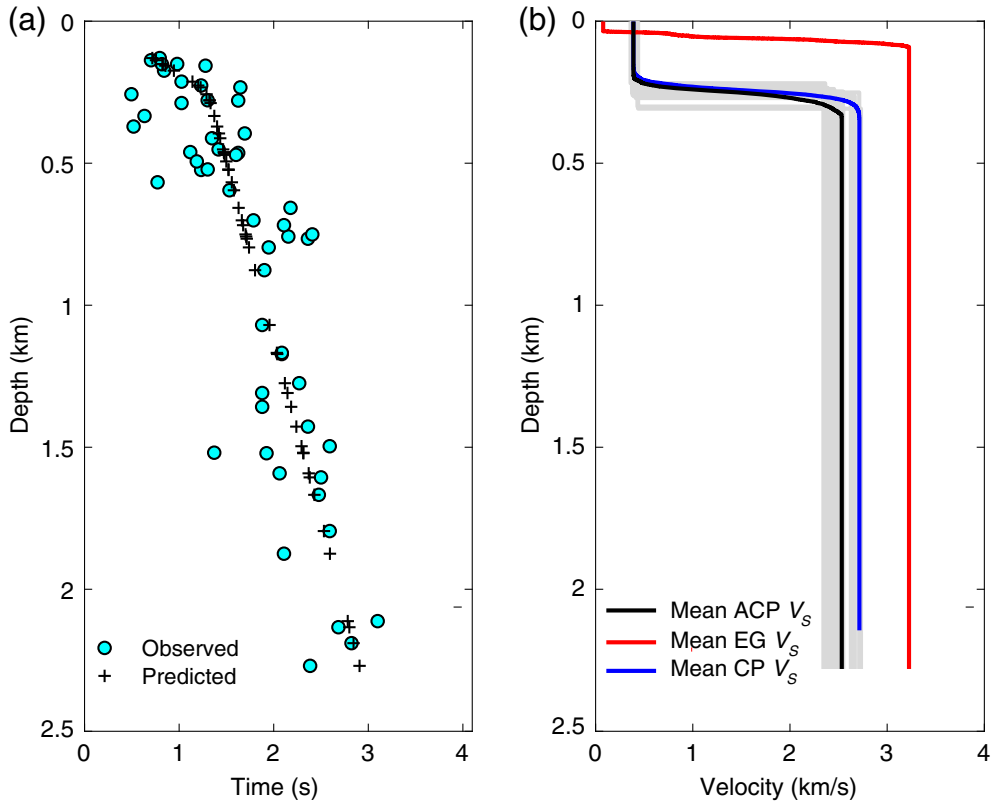

Figure 7. Two-layer V_S velocity profiles from inversion. (a) T_{Ss} measurements from and 4 Hz *Ps* RFs (cyan circles) compared to T_{Ss} predicted from the mean V_S profile from our best-fit inversion (black crosses). (b) V_S velocity inversions using T_{Ss} measurements and assuming V_S is composed of two layers. A range of velocity inversions using stations with sediment thickness less than 2.5 km is plotted in gray, and the average of the ensemble of models is plotted in black. The average of the ensemble of velocity profile obtained by inversion for the stations in the EG CP sediments is plotted in red, and for the stations in the CP is plotted in blue. The color version of this figure is available only in the electronic edition.

example stations with varying sediment thicknesses (Fig. 8b,c). For thin sediments and at frequencies typically used for receiver function analysis, the large amplitude PP_bs phase and the earlier arriving direct *P-to-S* sediment conversion, P_bs, may become indistinguishable from one another and overlap in time (Cunningham and Lekic, 2019). Therefore, we use high-frequency RFs (band-pass filtered 0.03–4 Hz), which allows for more accurate picks of T_{PPbs} that are better separated from P_bs arrivals in regions with thin sediments.

Measurements of T_{PPbs} and the PP_bs phase amplitude are made across the ACP. The same trends as with T_{Ss} are found including that the mean PRF agrees well with individual RFs at the same station. With increasing sediment thickness from west to east, T_{PPbs} increases (Fig. 9a, Fig. S2d). Deeper sediments will have faster velocities, reducing the impedance contrast between sediments and basement rock. As sediment thickness increases, as expected, the PP_bs phase amplitude decreases (Fig. 9b, Fig. S2e). This systematic behavior gives us confidence in the travel time and amplitude measurements of PP_bs made on high-frequency RFs. At stations with sediment thicknesses estimated to be greater than 1 km, the T_{PPbs} phase is small, and accurate picking of this phase becomes extremely challenging (Fig. 8c).

A V_P velocity profile is obtained assuming the same type of power-law relationship with depth used for V_S (Fig. S5); including the same misfit functions (equation 4), ε, and likelihoods. We invert for the V_P profile using all stations with sediments thickness of less than 2.5 km. We do not make an assumption about p, and find that this inversion prefers low exponents (p) than for V_S, and that the accepted models show more variation than those of the V_S profile; both a_1 and p are poorly constrained by the data (Fig. S6). The misfit reduction for the V_P power-law inversion for all of the stations greater than 2.5 km thickness is 53% compared to the stating model in which $a_1 = 100$, $V_0 = 1000$, and $p = 0.3$. Therefore, we repeat the inversions for V_P profiles, assuming that V_P increases linearly with depth. Assuming a linearly increasing V_P with depth, that is

$$z = V_0 + a_1(z), \tag{10}$$

in which V_0 is the V_P at the surface, and a_1 is the velocity gradient with depth, and $0 < a_1 < 2$. We perform the inversion on the three grouping of stations: EG, CP, and ACP. We find that V_P increasing linearly with depth better explains the data, and the average ensemble solution for the three velocity profiles are more similar (Fig. 10, Fig. S7); but produces velocities of V_P that are unrealistically high at depth Therefore, we calculate a V_P profile predicted by the average ensemble V_S profile (from the power-law relationship) using regression fit of Brocher (2005) (specifically, equation 9 in that study), which is valid for sedimentary lithologies with *S*-wave velocities less than 4.5 km/s. The "Brocher regression" V_P profile predicted from our V_S profiles is significantly different from both the V_P profiles calculated with the power-law relationship and linear relationship, but produces more reasonable *P*-wave velocity estimates at depth. This slower *P*-wave velocity at depth from

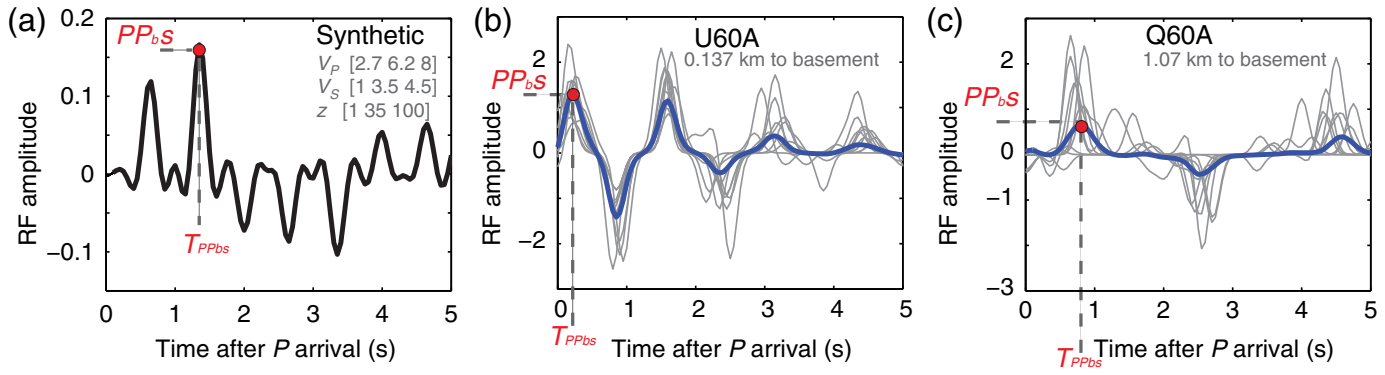

Figure 8. T_{PPbs} and PP_bs measurements from 4 Hz *Ps* receiver functions. With increasing sediment thickness, T_{PPbs} increases. (a) Synthetic RF calculated using spectral division for velocity model described in top right corner. T_{PPbs} and PP_bs are picked as the largest positive amplitude, shown by the dot. (b) 4 Hz *Ps* RFs for station U60A located on 0.137 km of sedimentary material. Mean *Ps* RF shown as thick (blue) line and a range of the 93 *Ps* RFs shown in gray. T_{PPbs} and PP_bs pick shown as dot. (c) 4 Hz *Ps* RFs for station Q60A located on 1.07 km of sedimentary material. Mean *Ps* RF shown as thick (blue) dot and a range of the 63 *Ps* RFs shown in gray. T_{PPbs} and PP_bs pick shown as dot. The color version of this figure is available only in the electronic edition.

the Brocher relationship does not estimate T_{PPbs} times between 1 and 2.5 km that are significantly different than the measured T_{PPbs} times at the same depths (Fig. 10), as the travel time of T_{PPbs} depends on both the average *S*- and *P*-wave velocity not the velocity at any specific depth. The difficulty we have in constraining reasonable *P*-wave velocities at depth is compounded by the difficulty of accurately picking the arrival time PP_bs at stations where the sedimentary strata are thicker than 1 km.

DISCUSSION AND VALIDATION

Measurements of fundamental frequency presented in this study agree with values observed in regions with similar sediment thickness (e.g., Parolai *et al.*, 2002; Pratt, 2018). For example, the fundamental frequency at station Y57A on shallow sediments (0.12 km) has a fundamental frequency of 1 compared to ~1 Hz predicted in Parolai *et al.* (2002) and ~1.1 Hz measured from HVSR in Pratt (2018). Station 356A on thick sediments (1.16 km) has a fundamental frequency of 0.28 Hz compared to 0.3 Hz and from Pratt (2018). However, when shallow unconsolidated sediments are present within the sedimentary strata, damaging amplification can also occur at higher frequencies. Most studies of fundamental frequency in the ACP measure the large amplification at the fundamental frequency from these shallow layers, which ranges from 1.5 to 12 Hz (e.g., Fischer *et al.*, 1995; Fairbanks *et al.*, 2008; Pratt *et al.*, 2017). Although significant in hazard analysis,

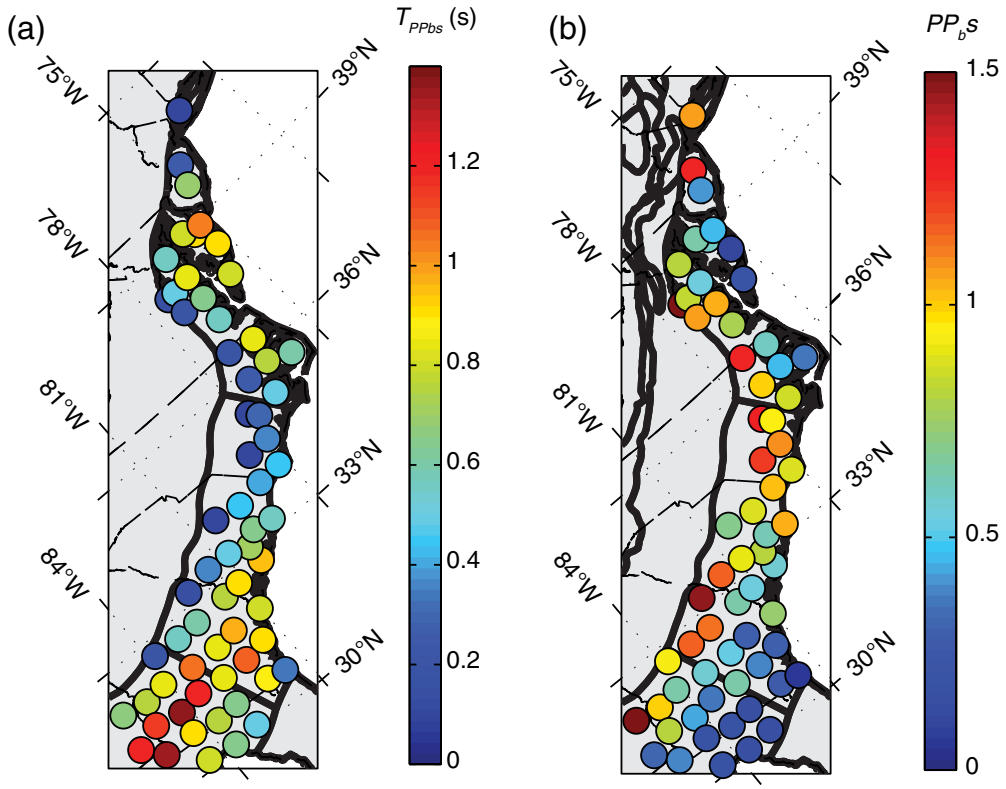

Figure 9. Measurements made from the 4 Hz RFs across the ACP. (a) Measurements of T_{PPbs} at each station across the ACP. As sediment thickness increases T_{PPbs} increases. (b) Measurements of PP_bs across the ACP. As sediment thickness increases, the amplitude of PP_bs (related to the impedance contrast) decreases. The color version of this figure is available only in the electronic edition.

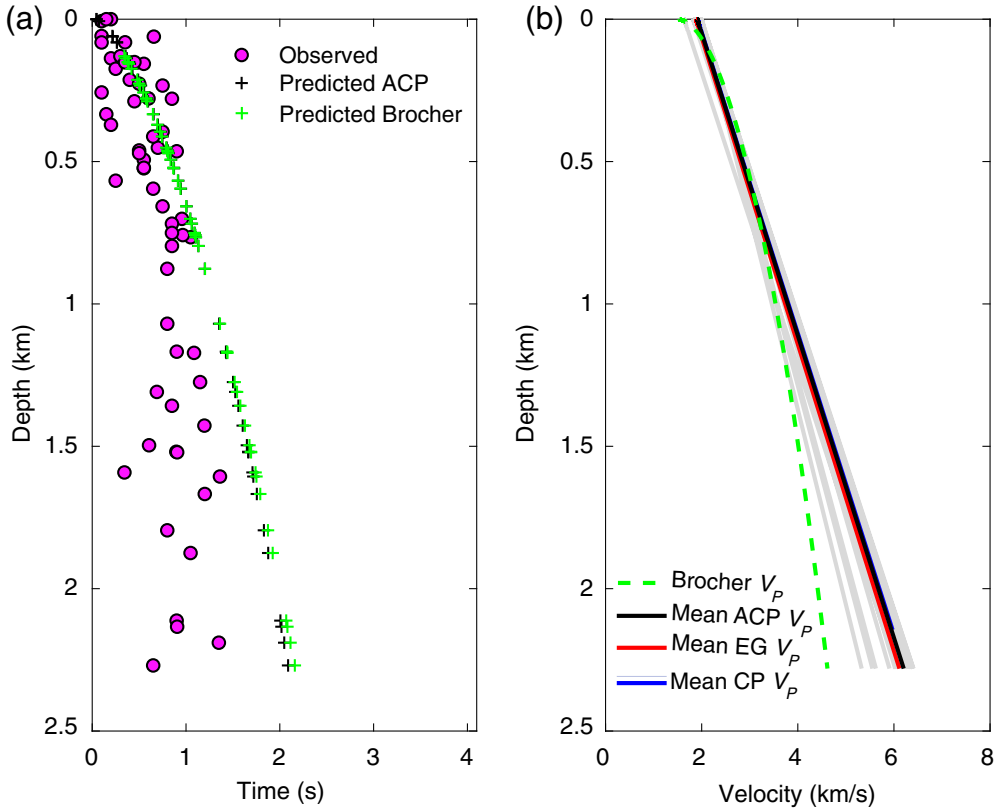

Figure 10. V_P velocity profile from inversion. (a) T_{PPbs} measurements from 4 Hz *Ps* RFs (magenta circles) compared to T_{PPbs} predicted from the mean V_P profile from our best-fit inversion (black crosses) and T_{PPbs} predicted from the Brocher (2005) relationship of V_P and V_S (green crosses). (b) V_P velocity inversions using T_{PPbs} measurements and assuming V_P increases in a linearly with depth. A range of velocity inversions using stations with sediment thickness less than 2.5 km is plotted in gray, and the average of the ensemble of models is plotted in black. The average of the ensemble of model velocity profiles from inversion for the stations in the EG CP sediments is plotted in red, and for the stations in the CP is plotted in blue. The V_P profile obtained from the Brocher (2005) relationship is plotted as a green dashed line. The linear relationships for V_P agree with each other but are not consistent with the Brocher (2005) regression relationship. The color version of this figure is available only in the electronic edition.

we focus our study solely on the peak amplification produced from sediment-bedrock impedance contrasts, which will contain lower frequency due to thicker sediments.

We could not identify any studies in the ACP that systematically map fundamental frequency throughout the ACP province. Therefore, we carry out two different analyses to validate that our measurements of T_{Ss} imply the same fundamental frequencies as would be obtained by more traditional methods. We identify a set of teleseismic earthquakes that are recorded at three stations with increasing sediment thickness. We then compute radial and transverse component spectral ratios using a method similar to the E-HVSR technique, in which the radial (R) and transverse (T) component multitaper power spectral density estimates are compared to the vertical (V) component multitaper power spectral density estimates event-by-event, in which the time-half-bandwidth product that controls the trade-off between spectral resolution and leakage is set to 4. We take the average at each station, and peaks in these ratios correspond to the resonant frequencies of the sediment and are shown in Figure 11. In addition, we compute a PRF spectral ratio, which is motivated by the SSR technique in which multitaper power spectral density estimates at stations on sediment are compared event-by-event to the mean spectrum of stations on bedrock where the time-half-bandwidth product is 4. Here, we choose as our bedrock reference stations the 11 stations determined to be in the ACP, but that do not have significant sediment contributions (as determined by the parameters detailed in Cunningham and Lekic, 2019, and discussed in the Receiver Function Calculations section). The PRF spectral ratios also exhibit peaks at frequencies corresponding to sediment resonances and are plotted in Figure 11. For stations U60A, Q59A, and Q60A with sediment thickness of 0.137, 0.534, and 1.07 km, respectively, our T_{Ss}-based fundamental frequency estimates are 0.71, 0.39, and 0.26 Hz, respectively. For these same stations, the E-HVSR and PRF spectral ratio techniques demonstrate that the peak amplification occurs at the same frequencies. As expected, the fundamental frequency using measurements of T_{Ss} is consistent with the peaks found in SSR and E-HVSR more traditional methods, showing increasing fundamental frequency with decreasing sediment thickness.

Using the *S*-reverberation time and the Brocher relationship, we inferred *S*- and *P*-wave velocity profiles for the ACP sediments above 2.5 km. We find that *S* velocities increase with the square root of depth, starting at very low wavespeed at the surface (0.1 km/s) and increasing to about 2.8 km/s at 2.5 km depth. Our estimates of V_S at 0.1–0.5 km agree with previous studies of the average *S*-wave velocity of the EG, CP, and central United States sediments of 0.45–0.67 km/s at the near surface (Chen *et al.*, 1996; Liu *et al.*, 1997; Bodin *et al.*, 2001; Pratt, 2018). We find that the EG, CP, and ACP *S*-wave velocity profiles are very similar to one

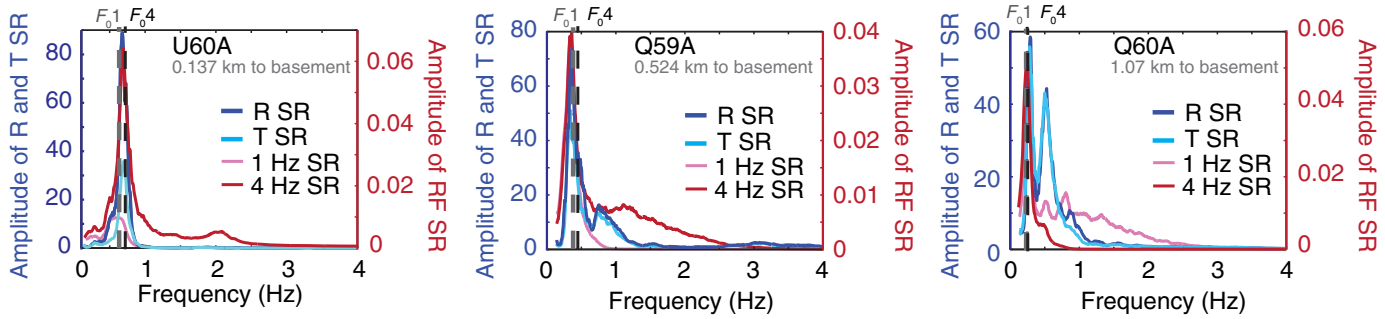

Figure 11. Comparison of site fundamental frequency ($F_0$4) measurements obtained in this study compared to more traditional spectral ratio techniques of estimating site fundamental frequency from peak amplitude. Earthquake horizontal-to-vertical spectral ratio (E-HVSR) techniques applied to radial (R, dark blue) and transverse (T, cyan) component data recorded at the seismic station to produce E and T spectral ratios (SRs). The blue *y* axis on the left applies to these E-HVSR techniques. Standard spectral ratio (SSR) techniques applied to *P-to-S* receiver function (PRF) data to create "PRF spectral ratios" using 1 (pink) and 4 Hz (red) PRFs. This produces 1 and 4 Hz SRs. The red y axis on the right applies to these SSR techniques. We perform this analysis for three stations which lie on sediment of differing thickness (U60A, Q59A, and Q60A). The color version of this figure is available only in the electronic edition.

another. This suggests that the strata in the ACP are similar and agree with previous studies (Cook *et al.*, 1981; Pratt, 2018). There are very few studies that constrain V_S velocity at depth, and so we turn to our V_P profiles to compare our results with other studies of the ACP velocity.

Both the power-law and linear inverted *P*-wave velocity profiles does not agree well with that predicted by the Brocher V_P/V_S regression, starting at ~3 km/s at the surface and increasing to ~6 km/s at 2.5 km depth, whereas the Brocher relationship estimates V_P at the surface to be closer to 0.3 km/s and ~4.5 at 2.5 km. Because of the fact that V_P is much greater than V_S in the shallow sediment (V_P/V_S is generally greater than 2), the *P*-leg of the PP_bs phase accumulates much less travel time than the *S*-leg. Therefore, when using any phase arrival visible on the PRF to infer V_P profiles, even small errors in picking can result in large errors in estimated V_P. The velocity estimates from the Brocher V_P profile in the shallow subsurface agrees well with previous estimates of V_P in the ACP, which suggests that V_P in the shallowest subsurface (<2 m) V_P is around 1.4 km/s (Yantis, 1983; Chapman *et al.*, 2003; Wells *et al.*, 2015). However, the velocities obtained using the Brocher relationship are slightly faster than studies at locations in ACP at depth. For example, at 0.8 km depth Chapman *et al.* (2003) an estimate of $V_P = 2.4$ km/s near Charleston, South Carolina, whereas our inversion suggests a faster average ACP V_P of ~3.2 km/s. In the Delmarva Peninsula, faster V_P velocities are found at depth from active source studies. For example, at 2.5 km depth Catchings *et al.* (2008) find that V_P ~4.5 km/*s* and *y* at 1.5 km depth, find that V_P ~3.5–4 km/s in agreement with our Brocher relationship at the same depths. Because our velocity profiles represent an average velocity in all of the ACP (similar to Pratt, 2018), it is difficult to directly compare our results to any one location, but instead we provide a regional velocity profile.

We further validate our velocity profiles by comparing the amplitudes of r_0 and measured directly on the PRF with amplitudes from the reflection and transmission coefficients calculated using the *S*-wave velocity profile obtained earlier. Having found that Brocher V_P/V_S scaling relationships are compatible with the data, we use density–V_S relationships to construct density profiles for the ACP. Together with crustal parameters of $V_P = 6.7$ km/s and density $= 2.69$ g/cm^3 from Next Generation Attenuation-East Project (Dreiling *et al.*, 2017), we use our V_S, and density profiles to calculate reflection and transmission coefficients for the *SS* reverberation (r_0) at each depth using expressions from Aki and Richards (2002). We find that the calculated $\grave{S}\acute{S}$ reflection coefficients have similar amplitude as the measured—r_0 at each station (Fig. S8), suggesting that the *S*-velocity profiles obtained are not only consistent with amplitude measurements not used in the inversion, but also that they may be expected to yield reasonable amplitude predictions when used in wave simulations. The relatively large variability in measured r_0 likely reflects variability in the lithology of the bedrock amalgamated in past collisions and accretionary events (Wagner *et al.*, 2018). If there was a systemic overestimate of predicted r_0 when compared to measured r_0, this method may be able to constrain the important attenuation or quality factor; however, no such trend is found as the measured r_0 values are too scattered.

Traditional SSR or HVSR techniques often use local earthquakes or the ambient noise field to measure site-specific sediment properties including fundamental frequency and site amplification. Although ambient noise techniques have shown great promise in improving data coverage in largely aseismic areas, the accuracy of the retrieved Green's functions depends on assumptions about the isotropic distribution of noise sources and stationarity of the signal (e.g., Tsai, 2009; Yao *et al.*, 2009). In the ACP, the dominant source of the seismic noise is the Atlantic Coast (e.g., Koper and Burlacu, 2015), resulting in a highly directional noise wavefield. This can introduce bias into phase and group velocity measurements made from

ambient noise cross correlations, necessitating the use of sophisticated adjoint methods for accurate retrieval of structure (e.g., Ermert *et al.*, 2017).

Because high-frequency receiver functions isolate the near-surface response from teleseismic recordings, existing broadband station deployments (such as USArray) can be used to characterize site-specific sediment fundamental frequency and regional velocity profiles across large geographic areas without relying on local seismicity or ambient noise. When the velocity contrast is significant, and the sedimentary layer is thick (greater than 0.1 km), *SS* reverberation phase arrivals are large and visible on the mean PRF with arrival times that increase, as expected, with increasing sediment thickness. However, relatively low-frequency band-pass corners of 0.5–1 Hz typically used in PRF studies of crustal structure are insufficiently high to distinguish between and interpret different phase arrivals (particularly P_bs and PP_bs) when sediment is less than 1 km thick, as is the case across much of the ACP (see Fig. S9). Here, we show that much higher frequency signals can be extracted from teleseismic PRFs, enabling the characterization of sediments as thin as 0.1 km. In regions where broadband stations have not been deployed or coverage is insufficient, receiver functions can be calculated from nodal array deployments (e.g., Ward and Lin, 2017; Liu *et al.*, 2018), which have optimal sensitivity in the frequency range of interest. Indeed, the ease of deployment and low cost of nodal deployment also enable targeted, detailed mapping of sedimentary sediments based on PRF technique.

PRFs are most often used to map interfaces within the deep crust and underlying mantle. However, interpreting PRF signals from deeper structures often requires accounting for signals due to sedimentary strata, yielding useful constraints on sediment structure as a byproduct. *S*-reverberation time (and sediment fundamental frequency) must be estimated when constructing shallow-layer reverberation removal filters, and *Ps* phases must be identified when applying shallow-layer corrections to *H-k* stacks (e.g., Yu *et al.*, 2015; Cunningham and Lekic, 2019). Therefore, *S*-wave velocity profiles can be calculated whenever PRFs are used in regions with significant sedimentary cover and independent measurements of sediment thickness. Although requiring more user interaction than traditional SSR or HVSR techniques, high-frequency PRFs may be useful in constraining sediment properties over large areas, especially in regions with low or intermittent seismic activity and highly directional noise wavefield.

Although PRFs are useful for constraining the fundamental frequency and *S*-wave velocity profile of thick sedimentary strata, picking the PP_bs phase to constrain *P*-wave velocity profiles is exceedingly challenging. As sediment thickness increases, the impedance contrast across the base of the sediment decreases and the amplitude of the PP_bs phase also decreases, making picking of the PP_bs phase in this region difficult in regions with sediment thicker than 1 km. In addition, although PRFs are not able to constrain all of the significant sedimentary basin properties important to hazard analysis including site-specific attenuation and amplification or at each station. The amplitudes of the measured *SS* reverberation show considerable scatter, and do not vary systematically from the predicted amplitudes calculated without accounting for attenuation (Fig. S9), suggesting that the PRF method is not sufficient to analyze CP attenuation or amplification.

CONCLUSIONS

Receiver function analysis of teleseismic events recorded at broadband seismic stations from USArray places constraints on fundamental frequency and allows determination of velocity profiles. We infer these sediment properties across the ACP from phase arrivals on high-frequency (4 Hz) PRFs. Using measurements of the two-way *S*-wave travel time on the receiver function, we map sediment fundamental frequency across the ACP. Although shallow sediment structure may result in even higher fundamental frequencies, the sediment fundamental frequencies presented in this work are consistent with sediment thickness and results from applying more traditional techniques to teleseismic data. In addition to providing site-specific fundamental frequencies, the relationship of T_{Ss} (or fundamental frequency) and sediment thickness may provide a method to estimate the expected fundamental frequency at any sediment thickness for thick sediments. The amplitudes measured on the RFs match expected patterns with increasing sediment thickness and associated decreasing sediment-bedrock impedance contrast. ACP, EG, and CP strata examined this study share a similar high-velocity profile for V_S until about 2.5 km depth, implying that above this depth, they share similar sediment structure. The V_S profile increases as the square root of depth, whereas V_P profiles are best explained by the Brocher regression fit. Receiver function amplitudes at the phase arrival times validate the V_S profiles.

DATA AND RESOURCES

We have included accompanying supplemental figures for this article, which are referenced in the text. The supplemental figures provide additional information regarding the measurements of T_{Ss} and T_{PPbs} made from the high-frequency PRFs including a plot of each station measurements versus basin thickness (Figs. S1, S2) and an example of making these phase arrival picks on PRFs with varying frequency content (Fig. S9). We have also included a figure of the amplitude measurements from PRFs compared to calculated refelction and transmission coefficients for the *S*-wave sediment velocity profile obtained in this study using Aki and Richards (2002) (Fig. S8). In addition to the information regarding the phase arrival picks, we provide supplemental figures of the *P*- and *S*-wave velocity profile inversion results that helped inform the chosen inversions used in the article (Figs. S3 and S5); as well as figures that show the velocity profile inversion parameter distributions (Figs. S4, S6, and S7). The waveform data used in this study were collected from Incorporated Research Institutions for Seismology (IRIS) Data Services

(http://ds.iris.edu/ds/, last accessed February 2017). The waveform data consists of three-component waveforms from 75 s before to 225 s after the *P*-arrival time for events with $M_w > 5.6$ at epicentral distances between 30° and 90° (processing methods detailed in Abt *et al.*, 2010). The events' list used to request waveform data was complied using earthquake magnitudes, locations, and depths were updated to those contained in the U.S. Geological Survey (USGS) Advanced National Seismic System (ANSS) composite catalog (http://earthquake.usgs.gov/data/comcat/, last accessed February 2017). The automatic quality-control procedure for calculating the *Ps* RFs is detailed in Abt *et al.* (2010). The dataset was culled to have a minimum Z-to-R cross correlation of 0.3, and a maximum difference of 25 s between the automatically determined arrival time and prediction for ak135 and did not use an additional signal-to-noise threshold for the *Ps* receiver functions. The free-surface transform of Kennett (1991) was used for estimating the upgoing *P–SV–SH* wavefield using surface velocities that minimize the correlation between upgoing *P* and *S* waveforms. The RFs are calculated using the free-surface transform matrix of Kennett (1991) and finding the surface velocity that minimizes the parent amplitude (*P* for *Ps* and *S* for *Sp*) on the daughter component to project the waveforms onto the *P–SV–SH* system; the arrival times are picked, and fourth-order Butterworth band-pass filter of 0.03–1 and 0.03–4 Hz is applied to the waveforms. We then use the iterative time-domain deconvolution with Gaussian half-amplitude half-width of ∼0.12 and ∼0.5 s for 4 and 1 Hz, respectively, to calculate the receiver functions in the time domain (Ligorria and Ammon, 1999). The 2010 population data were acquired from the Center for International Earth Science Information Network (CIESIN) (2018). Gridded Population of the World, Version 4 (GPWv4): Population Count, Revision 11. Palisades, New York: National Aeronautics and Space Administration (NASA) Socioeconomic Data and Applications Center (SEDAC; https://doi.org/10.7927/H4JW8BX5, last accessed July 2019). The peak ground acceleration (PGA) data in the same figure were acquired from the 2014 long-term hazard model of the USGS earthquake hazards program (https://earthquake.usgs.gov/hazards/hazmaps/conterminous/index.php#2014, last accessed July 2019). The 1D reference earth model ak135 was obtained from the IRIS data service products and can be downloaded through their website (https://ds.iris.edu/ds/products/emc-ak135-f/, last accessed January 2019).

ACKNOWLEDGMENTS

The authors would like to thank Martin Chapman, two anonymous reviewers, and Associate Editor Stefano Parolai for their comments and suggestions which greatly improved the article. The authors are especially grateful to Editor-in-Chief Thomas Pratt for his invaluable feedback and discussions which led to substantial improvements in the focus of this study. This work was supported by National Science Foundation (NSF) Grant CAREER EAR-1352214.

REFERENCES

Abrahamson, N., and W. Silva (2008). Summary of the Abrahamson & Silva NGA ground-motion relations, *Earthq. Spectra* **24,** no. 1, 67–97, doi: 10.1193/1.2924360.

Abt, D. L., K. M. Fischer, S. W. French, H. A. Ford, H. Yuan, and B. Romanowicz (2010). North American lithospheric discontinuity structure imaged by *Ps* and *Sp* receiver functions, *J. Geophys. Res.* **115,** no. 9, 1–24, doi: 10.1029/2009JB006914.

Aki, K., and P. G. Richards (2002). *Quantitative Seismology*, University Science Books, Sausalito, California.

American Association of Petroleum Geologists (AAPG). Basement RockProject Committee and U.S. Geological Survey (1967). Basement map of North America between latitudes 24° and 60° N, *U.S. Geol. Surv G62281*, available at https://www.loc.gov/resource/g3301c.ct003142/ (last accessed December 2018).

Baise, L. G., J. Kaklamanos, B. M. Berry, and E. M. Thompson (2016). Soil amplification with a strong impedance contrast: Boston, Massachusetts, *Eng. Geol.* **202,** 1–13, doi: 10.1016/J.ENGGEO.2015.12.016.

Bodin, P., K. Smith, S. Horton, and H. Hwang (2001). Microtremor observations of deep sediment resonance in metropolitan Memphis, Tennessee, *Eng. Geol.* **62,** nos. 1/3, 159–168, doi: 10.1016/S0013-7952(01)00058-8.

Borcherdt, R. (1970). Effects of local geology on ground motion near San Francisco Bay, *Bull. Seismol. Soc. Am.* **60,** no. 1, 29–61.

Brocher, T. (2005). Empirical relationship between elastic wavespeeds and density in the Earth's crust, *Bull. Seismol. Soc. Am.* **95,** no. 6, 2081–2092, doi: 10.1785/0120050077.

Catchings, R. D., D. S. Powars, G. S. Gohn, J. W. Horton Jr., M. R. Goldman, and J. A. Hole (2008). Anatomy of the Chesapeake Bay impact structure revealed by seismic imaging, Delmarva Peninsula, Virginia, USA, *J. Geophys. Res.* **113,** no. B08413, doi: 10.1029/2007JB005421.

Center for International Earth Science Information Network (CIESIN) (2018). Gridded population of the world, version 4 (GPWv4): Population count, Revision 11, Columbia University, NASA Socioeconomic Data and Applications Center (SEDAC), Palisades, New York, doi: 10.7927/H4JW8BX5 (last accessed July 2019).

Chapman, D. M. F., and O. A. Godin (2001). Dispersion of interface waves in sediments with power-law shear speed profiles. II. Experimental observations and seismo-acoustic inversions, *J. Acoust. Soc. Am.* **110,** no. 4, 1908–1916, doi: 10.1121/1.1401739.

Chapman, M. C., J. N. Beale, A. C. Hardy, and Q. Wu (2016). Modern seismicity and the fault responsible fo the 1886 Charleston, South Carolina, earthquake, *Bull. Seismol. Soc. Am.* **106,** no. 2, 364–372, doi: 10.1785/0120150221.

Chapman, M. C., P. Talwani, and R. C. Cannon (2003). Ground-motion attenuation in the Atlantic Coastal Plain near Charleston, South Carolina, *Bull. Seismol. Soc. Am.* **93,** 998–1011.

Chen, K.-C., J.-M. Chiu, and Y.-T. Yang (1996). Shear-wave velocity of the sedimentary basin in the upper Mississippi embayment using S-to-P converted Waves, *Bull. Seismol. Soc. Am.* **86,** no. 3, 848–856.

Chowns, T. M., and C. T. Williams (1983). Pre-cretaceous rocks beneath the Georgia Coastal Plain, in studies related to the Charleston, South Carolina Earthquake of 1886, *U.S. Geol. Surv. Profess. Pap.*, L1–L40.

Cook, F. A., L. D. Brown, S. Kaufman, J. E. Oliver, and T. A. Petersen (1981). COCORP seismic profiling of the Appalachian orogen beneath the coastal plain of Georgia, *Geol. Soc. Am. Bull.* **92,** no. 10, pt 1, 738–748, doi: 10.1130/0016-7606(1981)92<738:CSPOTA>2.0.CO;2.

Cunningham, E., and V. Lekic (2019). Constraining crustal structure in the presence of sediment: A multiple converted wave approach, *Geophys. J. Int.* **219,** no. 1, 313–327, doi: 10.1093/gji/ggz298.

Daniels, D. L., I. Zietz, and P. Popenoe (1983). Distribution of subsurface lower Mesozoic rocks in the southeastern United States as interpreted from regional aeromagnetic and gravity maps, *Studies Related to the Charleston, South Carolina, Earthquake of 1886—Tectonics and Seismicity: U.S. Geol. Surv. Profess. Pap.*, K1–K24.

Delgado, J., C. López Casado, J. Giner, A. Estévez, A. Cuenca, and S. Molina (2000). Microtremors as a Geophysical Exploration Tool: Applications and limitations, *Pure Appl. Geophys.* **157,** no. 9, 1445–1462, doi: 10.1007/PL00001128.

Dreiling, J., M. P. Isken, and W. D. Mooney (2017). Comparison of synthetic pseudoabsolute response spectral acceleration (PSA) for four crustal regions within central and Eastern North America (CENA), *Bull. Seismol. Soc. Am.* **107,** no. 1, 169–179, doi: 10.1785/0120160121.

Ermert, L., K. Sager, M. Afanasiev, C. Boehm, and A. Fichtner (2017). Ambient seismic source inversion in a heterogeneous Earth: Theory and application to the Earth's hum, *J. Geophys. Res.* **122,** 9184–9207, doi: 10.1002/2017JB014738.

Fairbanks, C. D., R. D. Andrus, W. M. Camp, and W. B. Wright (2008). Dynamic periods and building damage at Charleston, South Carolina during the 1886 earthquake, *Earthq. Spectra* **24,** no. 4, 867–888, doi: 10.1193/1.2980346.

Fenneman, N. M., and D. W. Johnson (1946). Physiographic divisions of the conterminous U.S., *Physiographic Committee Special Map*, U.S. Geological Survey, Reston, Virginia, available at https://water.usgs.gov/GIS/metadata/usgswrd/XML/physio.xml (last accessed December 2018).

Field, E. H., S. E. Hough, and K. H. Jacob (1990). Using microtremors to assess potential earthquake site response: A case study in Flushing Medows, New York City, *Bull. Seismol. Soc. Am.* **80,** no. 6, 1456–1480.

Fischer, K. M., L. A. Salvati, S. E. Hough, E. Gonzalez, C. E. Nelsen, and E. G. Roth (1995). Sediment-induced amplification in the Northeastern United States: A case study in Providence, Rhode Island, *Bull. Seismol. Soc. Am.* **85,** no. 5, 1388–1397.

Flores, J., O. Novaro, and T. H. Seligman (1987). Possible resonance effect in the distribution of earthquake damage in Mexico City, *Nature* **326,** no. 6115, 783–785, doi: 10.1038/326783a0.

Frankel, A. D., D. L. Carver, and R. A. Williams (2002). Nonlinear and linear site response and basin effects in Seattle for the M 6.8 Nisqually, Washington, earthquake, *Bull. Seismol. Soc. Am.* **92,** no. 6, 2090–2109, doi: 10.1785/0120010254.

Godin, O. A., and D. M. F. Chapman (2001). Dispersion of interface waves in sediments with power-law shear speed profiles. I. Exact and approximate analytical results, *J. Acoust. Soc. Am.* **110,** 1890, doi: 10.1121/1.1401776.

Hough, S. E. (2012). Initial assessment of the intensity distribution of the 2011 Mw 5.8 Mineral, Virginia, earthquake, *Seismol. Res. lett.* **83,** 649–657, doi: 10.1785/0220110140.

Joyner, W. B., R. E. Warrick, and T. E. Fumal (1981). The effect of quaternary alluvium on strong ground motion in the Coyote Lake, California, earthquake of 1979, *Bull. Seismol. Soc. Am.* **71,** no. 4, 1333–1349.

Kawase, H., F. Nagashima, K. Nakano, and Y. Mori (2018). Direct evaluation of S-wave amplification factors from microtremor H/V ratios: Double empirical corrections to "Nakamura" method, *Soil Dynam. Earthq. Eng.* 126**,** doi: 10.1016/j.soildyn.2018.01.049.

Kennett, B. L. N. (1991). The removal of free surface interactions from three-component seismograms, *Geophys. J. Int.* **104,** no. 1, 153–154, doi: 10.1111/j.1365-246X.1991.tb02501.x.

Kennett, B. L. N., E. R. Engdahl, and R. Buland (1995). Constraints on seismic velocities in the Earth from traveltimes, *Geophys. J. Int.* **122,** no. 1, 108–124, doi: 10.1111/j.1365-246X.1995.tb03540.x.

Kim, W., M. Gold, J. Ramsay, A. Meltzer, D. Wunsch, S. Baxter, V. Lekic, P. Goodling, K. Pearson, L. Wagner, *et al.* (2018). The Mw 4.2 Delaware earthquake of 30 November 2017, *Seismol. Res. Lett.* **89,** no. 6, 2447–2460, doi: 10.1785/0220180124.

Koper, K. D., and R. Burlacu (2015). The fine structure of double-frequency microseisms recorded by seismometers in North America, *J. Geophys. Res.* **120,** no. 3, 1677–1691, doi: 10.1002/2014JB011820.

Leahy, G. M., R. L. Saltzer, and J. Schmedes (2012). Imaging the shallow crust with teleseismic receiver functions, *Geophys. J. Int.* **191,** no. 2, 627–636, doi: 10.1111/j.1365-246X.2012.05615.x.

Lermo, J., and F. J. Chávez-García (1993). Site effect evaluation using spectral ratios with only one station, *Bull. Seismol. Soc. Am.* **83,** no. 5, 1574–1594.

Ligorria, J. P., and C. J. Ammon (1999). Iterative deconvolution and receiver-function estimation, *Bull. Seismol. Soc. Am.* **89,** no. 5, 1395–1400.

Liu, G., P. Persaud, and R. W. Clayton (2018). Structure of the northern Los Angeles Basins revealed in teleseismic receiver functions from short-term nodal seismic arrays, *Seismol. Res. Lett.* **89,** no. 5, 1680–1689, doi: 10.1785/0220180071.

Liu, H.-P., Y. Hu, J. Dorman, T.-S. Chang, and J.-M. Chiu (1997). Upper Mississippi embayment shallow seismic velocities measured in situ, *Eng. Geol.* **46,** nos. 3/4, 313–330, doi: 10.1016/S0013-7952(97)00009-4.

Nakamura, Y. (1989). A method for dynamic characteristics estimation of subsurface using microtremor on the ground surface, *Q. Rep. Railway Tech. Res. Inst.* **30,** no. 1, 25–33.

Narayan, J. P. (2010). Effects of impedance contrast and soil thickness on basin-transduced Rayleigh waves and associated differential ground motion, *Pure Appl. Geophys.* **167,** no. 12, 1485–1510, doi: 10.1007/s00024-010-0131-z.

Parolai, S., P. Bormann, and C. Milkereit (2002). New relationships between Vs, thickness of sediments, and resonance frequency calculated by the H/V ratio of seismic noise for the Cologne Area (Germany), *Bull. Seismol. Soc. Am.* **92,** no. 6, 2521–2527, doi: 10.1785/0120010248.

Perron, V., C. Gélis, B. Froment, F. Hollender, P.-Y. Bard, G. Cultrera, and E. M. Cushing (2018). Can broad-band earthquake site responses be predicted by the ambient noise spectral ratio? Insight from observations at two sedimentary basins, *Geophys. J. Int.* **215,** no. 2, 1442–1454, doi: 10.1093/gji/ggy355.

Petersen, M. D., M. P. Moschetti, P. M. Powers, C. S. Mueller, K. M. Haller, A. D. Frankel, Y. Zeng, S. Rezaeian, S. C. Harmsen, O. S. Boyd *et al.* (2014). Documentation for the 2014 update of the United States national seismic hazard maps, *U.S. Geol. Surv. Open-File Rept. 2014–1091*, 243 pp.; doi: 10.3133/ofr20141091.

Pitilakis, K., E. Riga, and A. Anastasiadis (2013). New code site classification, amplification factors and normalized response spectra based on a worldwide ground-motion database, *Bull. Earthq. Eng.* **11,** no. 4, 925–966, doi: 10.1007/s10518-013-9429-4.

Pratt, T. L. (2018). Characterizing and imaging sedimentary strata using depth-converted spectral ratios: An example from the Atlantic Coastal Plain of the Eastern United States, *Bull. Seismol. Soc. Am.* **108,** no. 5A, 2801–2815, doi: 10.1785/0120180046.

Pratt, T. L., T.-M. Brocher, C.-S. Weaver, K.-C. Miller, A.-M. Trhu, K.-C. Creager, R.-S. Crosson, and C.-M. Snelson (2003). Amplification of seismic waves by the Seattle basin, northwestern U.S., *Bull. Seismol. Soc. Am.* **93,** 533–545.

Pratt, T. L., J. W. Horton, J. Muñoz, S. E. Hough, M. C. Chapman, and C. G. Olgun (2017). Amplification of earthquake ground motions in Washington, DC, and implications for hazard assessments in Central and Eastern North America, *Geophys. Res. Lett.* **44,** no. 24, 12,150–12,160, doi: 10.1002/2017GL075517.

Sartain, S. M., and B. E. See (1997). The South Georgia Basin: An integration of landsat, gravity, magnetics and seismic data to delineate basement structure and Rift Basin geometry, *Gulf Coast Assoc. Geol. Soc. Trans.* **47,** 493–497.

Shearer, P. M., and J. A. Orcutt (1987). Surface and near-surface effects on seismic waves—Theory and borehole seismometer results, *Bull. Seismol. Soc. Am.* **77,** no. 4, 1168–1196.

Steidl, J. H., A. G. Tumarkin, and R. J. Archuleta (1996). What is a reference site?, *Bull. Seismol. Soc. Am.* **86,** no. 6, 1733–1748.

Stephenson, W. J., M. W. Asten, J. K. Odum, and A. D. Frankel (2019). Shear-wave velocity in the Seattle Basin to 2 km depth characterized with the krSPAC microtremor array method: Insights for urban basin-scale imaging, *Seismol. Res. Lett.* **90,** 1230–1242, doi: 10.1785/0220180194.

Tsai, V. C. (2009). On establishing the accuracy of noise tomography travel-time measurements in a realistic medium, *Geophys. J. Int.* **178,** no. 3, 1555–1564, doi: 10.1111/j.1365-246X.2009.04239.x.

Tsai, V. C., and S. Atiganyanun (2014). Green's functions for surface waves in a generic velocity structure, *Bull. Seismol. Soc. Am.* **104,** no. 5, 2573–2578, doi: 10.1785/0120140121.

van Der Baan, M. (2009). The origin of SH-wave resonance frequencies in sedimentary layers, *Geophys. J. Int.*, **178,** no. 3, 1587–1596.

Wagner, L., K. Fischer, R. Hawman, E. Hopper, and D. Howell (2018). The relative roles of inheritance and long-term passive margin lithospheric evolution on the modern structure and tectonic activity in the southeastern United States, *Geosphere* **14,** no. 4, 1385–1410, doi: 10.1130/GES01593.1.

Ward, K. M., and F.-C. Lin (2017). On the viability of using autonomous three-component nodal geophones to calculate teleseismic *Ps* receiver functions with an application to Old Faithful, Yellowstone, *Seismol. Res. Lett.* **88,** no. 5, 1268–1278, doi: 10.1785/0220170051.

Wells, D., J. A. Egan, D. G. Murphy, and T. Paret (2015). Ground shaking and structural response of the Washington monument during the 2011 Mineral, Virginia, earthquake, in *The 2011 Mineral, Virginia, Earthquake, and its Significance for Seismic Hazards in Eastern North America*, J. W. Horton, M. C. Chapman, and R. A. Green (Editors), doi: 10.1130/2015.2509(12).

Yantis, B. R., J. K. Costain, and H. D. Ackermann (1983). A reflection seismic study near Charleston, South Carolina, in *Studies Related to the Charleston, South Carolina, Earthquake of 1886—Tectonics and Seismicity*, G. S. Gohn (Editor), U.S. Geol. Surv. Profess. Pap. 1313, G1–G20.

Yao, H., X. Campman, M. V. de Hoop, and R. D. van der Hilst (2009). Estimation of surface wave Green's functions from correlation of direct waves, coda waves, and ambient noise in SE Tibet, *Phys. Earth Planet. In.* **177,** nos. 1/2, 1–11, doi: 10.1016/J.PEPI.2009.07.002.

Yassminh, R., A. Gallegos, E. Sandvol, and J. Ni (2019). Investigation of the regional site response in the Central and Eastern United States, *Bull. Seismol. Soc. Am.* **109,** 1005–1024, doi: 10.1785/0120180230.

Yeck, W. L., A. F. Sheehan, and V. Schulte-Pelkum (2013). Sequential H-stacking to obtain accurate crustal thicknesses beneath sedimentary basins, *Bull. Seismol. Soc. Am.* **103,** no. 3, 2142–2150, doi: 10.1785/0120120290.

Yilar, E., L. G. Baise, and J. E. Ebel (2017). Using H/V measurements to determine depth to bedrock and Vs30 in Boston, Massachusetts, *Eng. Geol.* **217,** 12–22, doi: 10.1016/J.ENGGEO.2016.12.002.

Yu, Y., J. Song, K. H. Liu, and S. S. Gao (2015). Determining crustal structure beneath seismic stations overlying a low-velocity sedimentary layer using receiver functions, *J. Geophys. Res.* **120,** no. 5, 3208–3218, doi: 10.1002/2014JB011610.

Zelt, B. C., and R. M. Ellis (1999). Receiver-function studies in the Trans-Hudson Orogen, Saskatchewan, *Can. J. Earth Sci.* **603,** 585–603, doi: 10.1139/e98-109.

Zhao, J. X., and H. Xu (2013). A comparison of VS 30 and site period as site-effect parameters in response spectral ground-motion prediction equations, *Bull. Seismol. Soc. Am.* **103,** no. 1, 1–18, doi: 10.1785/0120110251.

Manuscript received 29 July 2019
Published online 3 March 2020